AIP | Physics of Fluids

Absolute/convective instability of planar viscoelastic jets

Prasun K. Ray and Tamer A. Zaki

Citation: Physics of Fluids (1994-present) **27**, 014110 (2015); doi: 10.1063/1.4906441
View online: http://dx.doi.org/10.1063/1.4906441
View Table of Contents: http://scitation.aip.org/content/aip/journal/pof2/27/1?ver=pdfcov
Published by the AIP Publishing

PHYSICS OF FLUIDS **27**, 014110 (2015)

Absolute/convective instability of planar viscoelastic jets

Prasun K. Ray and Tamer A. Zaki[a)]
Department of Mechanical Engineering, Imperial College London, London, United Kingdom

(Received 27 March 2014; accepted 19 December 2014; published online 27 January 2015)

Spatiotemporal linear stability analysis is used to investigate the onset of local absolute instability in planar viscoelastic jets. The influence of viscoelasticity in dilute polymer solutions is modeled with the FENE-P constitutive equation which requires the specification of a non-dimensional polymer relaxation time (the Weissenberg number, We), the maximum polymer extensibility, L, and the ratio of solvent and solution viscosities, β. A two-parameter family of velocity profiles is used as the base state with the parameter, S, controlling the amount of co- or counter-flow while N^{-1} sets the thickness of the jet shear layer. We examine how the variation of these fluid and flow parameters affects the minimum value of S at which the flow becomes locally absolutely unstable. Initially setting the Reynolds number to $Re = 500$, we find that the first varicose jet-column mode dictates the presence of absolute instability, and increasing the Weissenberg number produces important changes in the nature of the instability. The region of absolute instability shifts towards thin shear layers, and the amount of back-flow needed for absolute instability decreases (i.e., the influence of viscoelasticity is destabilizing). Additionally, when We is sufficiently large and N^{-1} is sufficiently small, single-stream jets become absolutely unstable. Numerical experiments with approximate equations show that both the polymer and solvent contributions to the stress become destabilizing when the scaled shear rate, $\eta = \frac{We \frac{d\overline{U}_1}{dx_2}}{L}$ ($\frac{d\overline{U}_1}{dx_2}$ is the base-state velocity gradient), is sufficiently large. These qualitative trends are largely unchanged when the Reynolds number is reduced; however, the relative importance of the destabilizing stresses increases tangibly. Consequently, absolute instability is substantially enhanced, and single-stream jets become absolutely unstable over a sizable portion of the parameter space. © *2015 AIP Publishing LLC.* [http://dx.doi.org/10.1063/1.4906441]

I. INTRODUCTION

Polymer additives can have a substantial influence on the stability of free shear layers. While much of the work in this area has focused on cylinder wakes,[1–4] the temporal stability of polymeric mixing layers[5] and jets[6] has also been investigated. Generally, these works found viscoelasticity to be stabilizing although the degree of stabilization can depend on the constitutive equation used to model the influence of the polymer on the flow.[5] Recently, the present authors investigated absolute instability in spatially developing mixing layers of dilute polymer solutions.[7] There, we found that viscoelasticity can, in some cases, have a substantial destabilizing influence. The presence and strength of this destabilization depend on the choice of constitutive model as well as the flow and fluid parameters. Results with the widely used but simplistic Oldroyd-B model showed substantial destabilization which can be understood with a modestly modified version of the long-wave analysis

a)Present address: Department of Mechanical Engineering, Johns Hopkins University, Baltimore, MD 21218, USA. Electronic mail: t.zaki@jhu.edu

presented by Azaiez and Homsy.[5] Results obtained with the more-realistic FENE-P model showed more complicated behavior, and depending on the problem parameters, viscoelasticity can be stabilizing or destabilizing. Somewhat surprisingly, we found that reducing the Reynolds number could have a destabilizing effect due to a shift towards "Oldroyd-B behavior."

The relative simplicity of the mixing layer is helpful for developing a basic understanding of the influence of viscoelasticity on instability mechanisms. However, it is important to consider more realistic flows such as jets and wakes as well. Here, we investigate the onset of local absolute instability in plane viscoelastic jets. Moving from mixing layers to jets results in a tangible increase in complexity. With the jet, there is an external length scale, and the shear-layer thickness must be specified. Furthermore, there are multiple instability modes to consider.[8] There is a "shear-layer mode" which is similar to the instability of the mixing layer, and there is a series of "jet-column modes" which are influenced by the width of the jet. Additionally, each of these modes may be sinuous or varicose depending on their symmetry relative to the jet centerline. One must also distinguish between jets exiting straight ducts and converging nozzles. Rallison and Hinch[6] (RH) considered the former case in their study of the temporal stability of single-stream Oldroyd-B jets with parabolic velocity profiles. They showed that elasticity was generally stabilizing in planar jets, and explained and contrasted the instability mechanisms of varicose and sinuous modes. Here, we aim to build on their foundational work, and consider the stability of co- and counter-flowing jets with a range of shear-layer thicknesses. Thin shear-layer velocity profiles resemble the "tophat" profiles found near the exit of a converging nozzle, while thicker profiles are expected to produce results similar to those obtained with a parabolic profile. Two other important differences from Rallison and Hinch are that we primarily use the FENE-P model which accounts for the finite-extensibility of polymer molecules and produces shear-thinning, and we focus on spatiotemporal instabilities which allow us to demarcate regions of absolute and convective instability.

Our analysis assumes that the base flow is slowly spreading and uses local absolute/convective stability theory.[9] Our focus is on the onset of absolute instability which leads to perturbations growing exponentially in time at the point of excitation. Yu and Monkewitz[10] applied this approach to variable density Newtonian jets. They found that single-stream uniform-density jets are not absolutely unstable. However, the (first) varicose jet-column mode does become absolutely unstable when the density of the jet is sufficiently small (see also the experimental study, Yu and Monkewitz[11]). Rees and Juniper[12] used a similar methodology to show that confinement enhances absolute instability in Newtonian jets (and wakes). In this study, we assess the influence of viscoelasticity on absolute instability in constant-density, unconfined polymeric jets. The governing equations and numerical methodology are described in Sec. II. Then, we present and analyze numerical results which illustrate the influence of viscoelasticity on jet stability. The fundamental question of interest is whether viscoelasticity enhances or suppresses absolute instability in planar jets. The numerical results presented below address this question while providing insight into the mechanisms which drive the most significant non-Newtonian effects. Ultimately, the desirability of a stabilizing or destabilizing effect is application-dependent. Destabilization can enhance mixing and thus be beneficial. Alternatively, for submerged jets, cavitation (and its associated noise) can be a significant problem, and stabilization of the jet is desirable. Also of interest are drag-reduced turbulent shear flows which have received sustained interest over several decades.[13] In realistic, complex flow configurations, shear layers may separate, and a clear understanding of the stability properties of canonical viscoelastic free shear layers should guide the analysis and control of these more-complex flows.

II. FORMULATION AND METHODOLOGY

The formulation and methodology used here are similar to those presented in Ray and Zaki.[7] We begin with the Navier-Stokes equations for incompressible flow modified with a "polymer-stress" term to account for the influence of polymers on the flow

$$\frac{\partial u_j}{\partial x_j} = 0, \tag{1a}$$

$$\frac{\partial u_i}{\partial t} + u_j \frac{\partial u_i}{\partial x_j} + \frac{\partial p}{\partial x_i} = \frac{\beta}{Re} \frac{\partial^2 u_i}{\partial x_j \partial x_j} + \frac{1-\beta}{Re} \frac{\partial a_{ji}}{\partial x_j}, \tag{1b}$$

where u_i is velocity, p is pressure, and $\frac{1-\beta}{Re} a_{ij}$ is the polymer stress. The Reynolds number is $Re = \frac{U_0 h}{\nu}$, where the velocity scale, U_0, is the average of the free-stream and centerline velocities, and the length scale, h, is the jet half-width. The kinematic viscosity of the solution is ν, while the ratio of the solvent and solution viscosities is $\beta = \frac{\nu_s}{\nu}$. We have assumed that density is uniform and constant. We will primarily use the FENE-P constitutive model to compute the polymer stress,

$$\frac{\partial c_{ij}}{\partial t} + u_k \frac{\partial c_{ij}}{\partial x_k} - c_{ik} \frac{\partial u_j}{\partial x_k} - c_{kj} \frac{\partial u_i}{\partial x_k} = -a_{ij}, \tag{2a}$$

$$a_{ij} = \frac{1}{We} \left(\frac{L^2 - 3}{L^2 - c_{kk}} c_{ij} - \delta_{ij} \right), \tag{2b}$$

where $We = \frac{\lambda U_0}{h}$ is the Weissenberg number, λ is a polymer relaxation timescale, and L is closely related to the maximum polymer length, R_0: $L^2 = R_0^2 + 3$. Here, L and R_0 have been non-dimensionalized with the molecular length scale, $\sqrt{k_B T/H}$, where k_B is the Boltzmann constant, T is the fluid temperature, and H is a Hookean spring constant. The conformation tensor, c_{ij}, has been non-dimensionalized with $(k_B T/H)\frac{R_0^2}{R_0^2+3}$, and with these scalings, $c_{ij} = \delta_{ij}$ at equilibrium (see the Appendix of Ref. 14 for further details). The Oldroyd-B model equations are recovered from Eq. (2) by taking the limit $L \to \infty$. The FENE-P model is based on a kinetic theory in which polymers are modeled as beads connected by nonlinear, finitely extensible springs. In steady shear flow with velocity gradient, $\frac{d\overline{U}_1}{dx_2}$, the behavior of these springs depends on the scaled shear rate,[7,15] $\eta = \frac{We \frac{d\overline{U}_1}{dx_2}}{L}$. At small shear rates, the springs behave linearly, and the FENE-P and Oldroyd-B models produce similar results. When η is large, the springs become elongated and stiffen resulting in an attenuation of the polymer stress. The FENE-P model is far from perfect—see Zhou and Akhavan[16] and references therein for information on its applicability and limitations—but, unlike the Oldroyd-B model, it accounts for the finite extensibility of polymer molecules and produces shear thinning. The FENE-P model also seems to have become the model-of-choice for numerical simulations of inertial viscoelastic flows,[3,13] and its use here should facilitate comparisons between simulations and our stability results. Further background on the FENE-P model can be found in Bird *et al.*[17]

We proceed by decomposing the flow into a steady, parallel base state, and small-amplitude perturbations, $f = \overline{F}(x_2) + f'(x_i,t)$. Then, after linearizing the equations and assuming that perturbations take the form, $f' = \tilde{f}(x_2)e^{i(\alpha x_1 - \omega t)}$, the governing equations can be written as

$$\mathbf{A}\tilde{f} = \mathbf{B}\frac{d\tilde{f}}{dx_2}, \tag{3}$$

with $\tilde{f} = \left[\tilde{u}_1 \ \frac{d\tilde{u}_1}{dx_2} \ \tilde{u}_2 \ \tilde{p}\right]^T$. Expressions for $\mathbf{A}$ and $\mathbf{B}$ are given in the Appendix, and we restrict this study to two-dimensional instabilities. The base-state velocity profiles are given by

$$\overline{U}_1 = 1 - S + \frac{2S}{1 + \left(2^{x_2^2} - 1\right)^N}. \tag{4}$$

The velocity of the free stream is $1 - S$, so when $S < 1$, the jet is co-flowing, while $S > 1$ gives counterflow. The shear-layer thickness is set by N^{-1}. The dependence of the momentum thickness, δ, on N^{-1} and a few illustrative profiles are shown in Figure 1. This family of velocity profiles was used by Meliga *et al.*[18] (see also Monkewitz[19]) in their study of axisymmetric wakes, while Rees and Juniper[12] used a form of these profiles modified for confinement in their study of planar jet and wake stability. The base-state polymer stress components for a parallel FENE-P shear flow are

$$\overline{A}_{11} = 2\frac{We}{\mathcal{F}(\eta)^2}\left(\frac{d\overline{U}_1}{dx_2}\right)^2, \ \overline{A}_{12} = \frac{1}{\mathcal{F}(\eta)}\frac{d\overline{U}_1}{dx_2}, \ \overline{A}_{22} = 0. \tag{5}$$

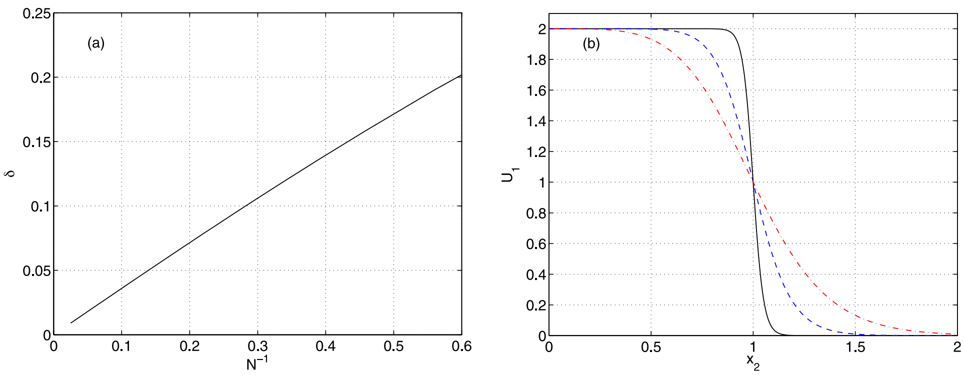

FIG. 1. Base flow, S = 1; (a) momentum thickness; (b) velocity profiles; ——, $N^{-1} = 0.07$; — —, $N^{-1} = 0.25$; – · –, $N^{-1} = 0.5$.

The function $\mathcal{F}(\eta)$ is defined as,[20] $\mathcal{F} \equiv \frac{\sqrt{3}\eta}{2\sinh(\phi/3)}$, where $\phi = \sinh^{-1}\left(3\sqrt{\frac{3}{2}}\eta\right)$. The influence of nonlinear elasticity on the base-state polymer stress is represented by $\mathcal{F}(\eta)$, and Figure 2 shows $1/\mathcal{F}(\eta)^2$. The figure also includes the large-η approximation, $1/\mathcal{F}(\eta)^2 \approx (2\eta^2)^{-2/3}$, which is used in the analysis below.

The locally parallel base flow assumption applied here has been widely used in Newtonian flow-stability studies (e.g., Michalke,[21] Huerre and Monkewitz,[9] and references therein), and the assumption requires the relative change in the base state over an instability wavelength to be small. For Newtonian flows, this requirement is satisfied if the Reynolds number is sufficiently large, but for polymeric flows, we must also consider streamwise variations associated with viscoelastic effects. Rallison and Hinch[6] and Hinch[5] considered this problem in detail, and following their analysis,viscoelastic non-parallel effects will be driven by stress relaxation (with time scale, λ) and elastic shear waves (with velocity scale, $c_s = \sqrt{\nu/\lambda}$). The locally parallel assumption for spatially growing waves then requires, $\alpha\, We \gg 1$ and $M_s \alpha \delta \gg 1$, where $M_s = \frac{U_0}{c_s} = \sqrt{Re\, We}$ is the visco-elastic Mach number. We will examine a large parameter space which in some cases will require the relaxation of these requirements. In such cases, we cannot expect quantitative accuracy but aim to establish the basic qualitative trends associated with viscoelastic effects. A similar approach has proven to be useful in studies of Newtonian flows where tangible non-parallel effects are present.[22–24]

The approach used here to search for absolute instability is similar to that used by Monkewitz[22] in his study of wake instabilities governed by the Orr-Sommerfeld equation. We use a shooting method with re-orthonormalization[25] to integrate Eq. (3). A symmetry condition is enforced to initiate integration from $x_2 = 0$; for sinuous modes, $\tilde{u}_1(x_2 = 0) = \tilde{p}(x_2 = 0) = 0$ while varicose modes require, $\tilde{u}_2(x_2 = 0) = \frac{d\tilde{u}_1}{dx_2}(x_2 = 0) = 0$. We search for saddle points where the complex

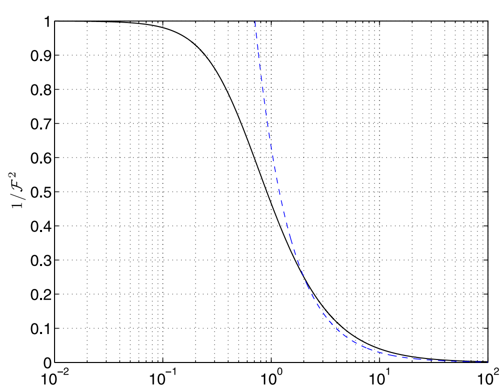

FIG. 2. ——, FENE-P function, $1/\mathcal{F}(\eta)^2$; — —, large-η approximation.

frequency and wavenumber ($\omega = \omega_0$ and $\alpha = \alpha_0$, respectively) satisfy $\frac{d\omega}{d\alpha}|_{(\alpha_0,\omega_0)} = 0$. These saddle points are required to correspond to the pinching of upstream- and downstream-propagating spatial branches, and they determine the long-time asymptotic behavior of the impulse response of the jet. The flow is absolutely unstable if the imaginary part of ω_0 is positive.[9,26]

III. RESULTS

Our numerical results show the influence of the flow and fluid parameters on the critical value of S at which absolute instability first appears (where the imaginary part of ω_0 is zero). In the results shown below, the jet is absolutely unstable when $S > S_{crit}$. We compute S_{crit} for the first jet-column and shear-layer modes with both varicose and sinuous symmetries to find which mode-type gives the smallest value of S_{crit} and thus dictates the presence of absolute instability. The influence of viscoelasticity on this "most-dangerous" mode is then examined in detail, and we are particularly interested in cases where $S_{crit} \le 1$, as this indicates the appearance of absolute instability in single-stream and co-flowing jets due to viscoelasticity (single-stream uniform-density Newtonian jets are not absolutely unstable[10]). We will initially focus on cases where the viscosity ratio, Reynolds number, and maximum extensibility are set to $L = 100$, $\beta = 0.7$, and $Re = 500$. Simulations[27,28] of channel flows with high- and maximum drag reduction typically use values of L between 60 and 120. Additionally, this choice of parameters is in line with our basic modeling assumptions—β should be close to one for dilute solutions, Re should be "large" for a locally parallel base flow approximation—and leads to results where viscoelasticity has a clear, tangible influence on jet stability. Later, we will show how the variation of β, Re, and L affects S_{crit}.

The jet-column modes are examined in Figure 3. The results show the influence of the jet shear-layer thickness and the Weissenberg number on S_{crit} and the real part of the instability wavenumber, $\alpha_{r,crit}$, for different Weissenberg numbers. S_{crit} is smaller for the varicose mode over the entire parameter space shown, and increasing We reduces S_{crit} for this mode when $N^{-1} \lesssim 0.25$. This destabilizing influence is most dramatic for small values of N^{-1}. As a result, the region of local absolute instability for a given value of S shifts towards thinner shear layers (i.e., towards the jet nozzle), and increasing We to 5 leads to the appearance of absolute instability in a single-stream jet when $N^{-1} < 0.0308$.

Results for the varicose and sinuous shear-layer modes are shown in Figure 4. It is straightforward to distinguish the shear-layer mode from jet-column modes when the shear layer is thin. The wavelength of the shear-layer mode is then substantially smaller than the wavelengths of the jet-column modes, and there is also a greater sensitivity to the shear-layer thickness. However, when the thickness is sufficiently large ($N^{-1} \gtrsim 0.12$), the shear-layer mode merges into a jet-column mode. This transition typically occurs when $\alpha_r \approx 3$, which roughly corresponds to the instability wavelength matching the jet width. The irregular shape of the $\alpha_{r,crit}$ curves when $N^{-1} \gtrsim 0.12$

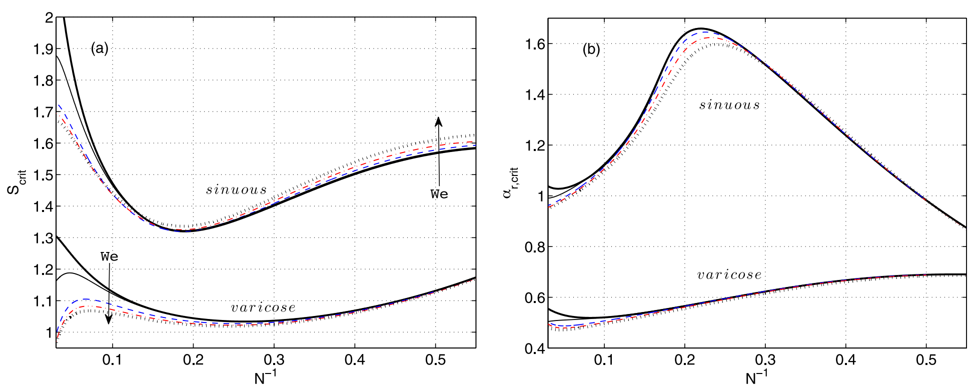

FIG. 3. Influence of We and N^{-1} on absolute instability of the first jet-column mode, $Re = 500$, $\beta = 0.7$, $L = 100$; —— (thick), Newtonian; ——, $We = 1$; — —, $We = 5$; – · –, $We = 10$; ·, $We = 20$. (a) S_{crit}; (b) $\alpha_{r,crit}$.

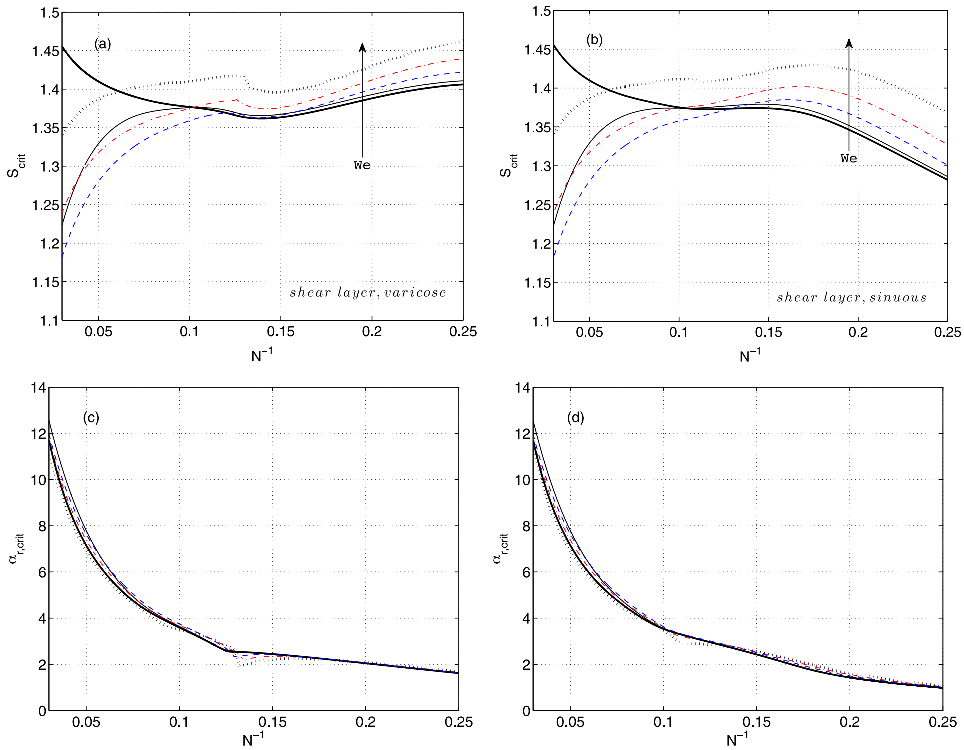

FIG. 4. Influence of *We* and N^{-1} on absolute instability of the shear-layer mode, *Re* = 500, β = 0.7, *L* = 100; —— (thick), Newtonian; ——, *We* = 1; — —, *We* = 5; – · –, *We* = 10; · · ·, *We* = 20. (a) and (c), varicose; (b) and (d), sinuous.

(Figures 4(c) and 4(d)) is caused by this merging of modes. These complexities do not have significant implications: comparing Figures 4(a) and 3(a) shows that it is the first varicose jet-column mode which determines the onset of absolute instability.

Figure 5(a) shows the influence of the elasticity, $E^*_\delta = \frac{(1-\beta)We_\delta}{Re_\delta}$, on S_{crit} for the first sinuous and varicose jet-column modes as well as the sinuous and varicose shear-layer modes when $N^{-1} = 0.07$ (and $\delta = 0.025$). The δ subscript indicates that the momentum thickness has been used as the reference length scale. This allows us to directly compare mixing-layer stability results with the jet modes, and the S_{crit} curve for a tanh mixing layer (computed using the methodology described

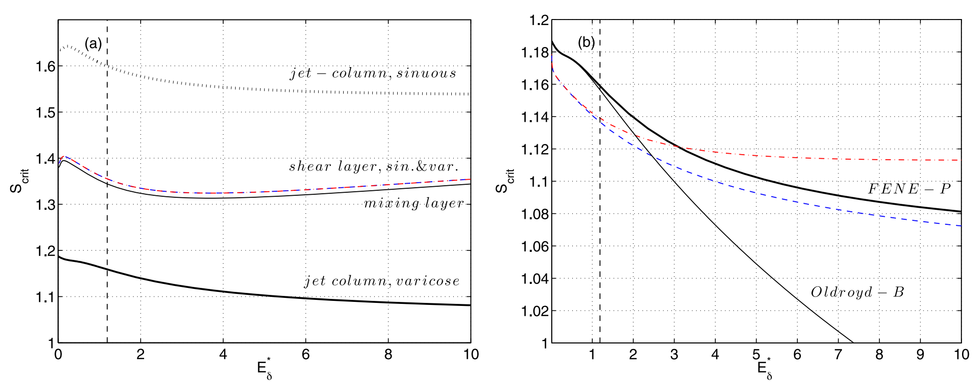

FIG. 5. Influence of elasticity on S_{crit}, *Re* = 500, β = 0.7, *L* = 100; N^{-1} = 0.07, *Re* = 500; (a) —— (thick), varicose jet-column mode; ——, tanh mixing layer; — —, varicose shear-layer mode; – · –, sinuous shear-layer mode; · · ·, sinuous jet-column mode; (b) varicose jet-column mode: ——, Oldroyd-B; —— (thick), FENE-P; — —, FENE-P with stress approximation; – · –, FENE-P with modified stress approximation; vertical dashed line, $\frac{We_\delta}{L} = 0.5$.

in Ray and Zaki[7]) is included in the figure. The sinuous and varicose shear-layer mode results are essentially identical, and they are very close to the mixing layer result. When the shear layer is thin, the jet width and centerline symmetry condition are practically irrelevant for the shear-layer modes. Figure 5(a) also shows the importance of the varicose jet-column mode as S_{crit} is distinctly larger for the other modes. We will now primarily focus on the behavior of the (first) varicose jet-column mode when the shear layer thickness is small, taking $N^{-1} = 0.07$ as a representative case.

A. Varicose jet-column mode (thin shear layer)

Large-Weissenberg number approximations for the polymer stress provide a helpful framework for understanding how the varicose jet-column mode is influenced by viscoelasticity. Assuming that $|\alpha| We \gg 1$, $L \gg 1$, and $|\alpha| \lesssim O(1)$, the polymer stress components can be approximated as

$$\tilde{a}_{11} \approx \left(\frac{2\eta^2}{\mathcal{F}} + \mathcal{F}\right)\left[\frac{2}{\mathcal{F}}\overline{A}_{11}\frac{d\Phi}{dx_2} + \frac{1}{We}\frac{d\overline{C}_{11}}{dx_2}\Phi\right], \ \tilde{a}_{12} \approx -i\alpha\overline{A}_{11}\Phi, \ \tilde{a}_{22} \approx 0, \tag{6}$$

where $\Phi = \frac{-i\alpha\tilde{u}_2}{\tilde{U}}$, $\tilde{U} = \overline{U}_1 - c$, and $c = \frac{\omega}{\alpha}$. Equation (6) is identical to the long-wave stress approximation introduced in Ray and Zaki.[7] With this approximation, the linearized momentum equations can be written as

$$\left[\tilde{U}^2 - \frac{2E^*}{\mathcal{F}^2}\left(\frac{d\overline{U}_1}{dx_2}\right)^2\left(1 + 4\frac{\eta^2}{\mathcal{F}^2}\right)\right]\frac{d\Phi}{dx_2} + \tilde{p} = \frac{\beta}{i\alpha\, Re}\left[\frac{d^3(\tilde{U}\Phi)}{dx_2^3} - \alpha^2\frac{d(\tilde{U}\Phi)}{dx_2}\right], \tag{7a}$$

$$\alpha^2\left[\tilde{U}^2 - \frac{2E^*}{\mathcal{F}^2}\left(\frac{d\overline{U}_1}{dx_2}\right)^2\right]\Phi + \frac{d\tilde{p}}{dx_2} = -\frac{i\alpha\beta}{Re}\left[\frac{d^2(\tilde{U}\Phi)}{dx_2^2} - \alpha^2\tilde{U}\Phi\right], \tag{7b}$$

and we have replaced the base-state normal stress using, $\frac{(1-\beta)}{Re}\overline{A}_{11} = \frac{2E^*}{\mathcal{F}^2}\left(\frac{d\overline{U}_1}{dx_2}\right)^2$. We are primarily interested in the terms on the left-hand sides of the equations which contain the elasticity, E^*. When the shear rate, η, is zero, approximations for the Oldroyd-B model introduced by Azaiez and Homsy[5] are recovered. More generally, we can anticipate that results obtained with the FENE-P and Oldroyd-B models will be similar when η is sufficiently small. Indeed, results for FENE-P and Oldroyd-B mixing layers[7] are similar when the constraint, $\frac{We_\delta}{L} \lesssim 0.5$, is satisfied ($\frac{We_\delta}{L}$ is used instead of η since S_{crit} is a dependent variable). Oldroyd-B and FENE-P results for the varicose jet-column mode are compared in Figure 5(b). As in the mixing layer, when $\frac{We_\delta}{L} \lesssim 0.5$, the FENE-P result is close to the Oldroyd-B curve. Within this "Oldroyd-B region," approximate momentum equations (7) indicate that the influence of viscoelasticity is dictated by the balance between inertial ($\tilde{U}^2$) and polymer stress ($\frac{(1-\beta)}{Re}\overline{A}_{11}$) terms. When the elasticity, E^*_δ, is $O(1)$, the magnitudes of these terms are similar, and viscoelasticity has a destabilizing influence reducing S_{crit} for all four modes in Figure 5(a). However, at larger values of the elasticity, when $\frac{We_\delta}{L} \gtrsim 0.5$, the shear-layer and jet-column mode results are different. The shear-layer mode tracks the mixing layer behavior, while the jet-column mode continues to be destabilised by elasticity.

Finite shear-rate effects tend to attenuate the base-state polymer stress while amplifying the streamwise-normal perturbation polymer stress. At large shear rates, $\mathcal{F}(\eta) \approx (2\eta^2)^{1/3}$. It follows that $\overline{A}_{11} \approx \left(\frac{2}{\eta}\right)^{1/3} L\frac{d\overline{U}_1}{dx_2}$, and the attenuating influence of the shear rate on $\overline{A}_{11}$ is evident. Comparing the large-We approximation for $\tilde{a}_{11}$ (Eq. (6)) with the viscoelastic term in Eq. (7(a)) leads us to focus on the $(4\frac{\eta^2}{\mathcal{F}^2})\overline{A}_{11}\frac{d\Phi}{dx_2}$ contribution to $\tilde{a}_{11}$. When η is large, $(4\frac{\eta^2}{\mathcal{F}^2})\overline{A}_{11} \approx (32\eta)^{1/3}L\frac{d\overline{U}_1}{dx_2}$, so increasing η increases the influence of $\tilde{a}_{11}$ even though $\overline{A}_{11}$ is attenuated. The importance of this increase is shown in Figure 5(b) where solutions to the full stability equations for the varicose jet-column mode are compared to solutions of complete Eq. (7) and Eq. (7) with the $\left(4\frac{\eta^2}{\mathcal{F}^2}\right)\overline{A}_{11}\frac{d\Phi}{dx_2}$ term removed. First, we note that the large-We equations provide a good approximation to the full solution. Then, comparing the two approximate solutions, we see that the amplification of $\tilde{a}_{11}$ is destabilizing as it produces a reduction in S_{crit}. It should be noted that the effect of $\tilde{a}_{11}$ is not always destabilizing. For

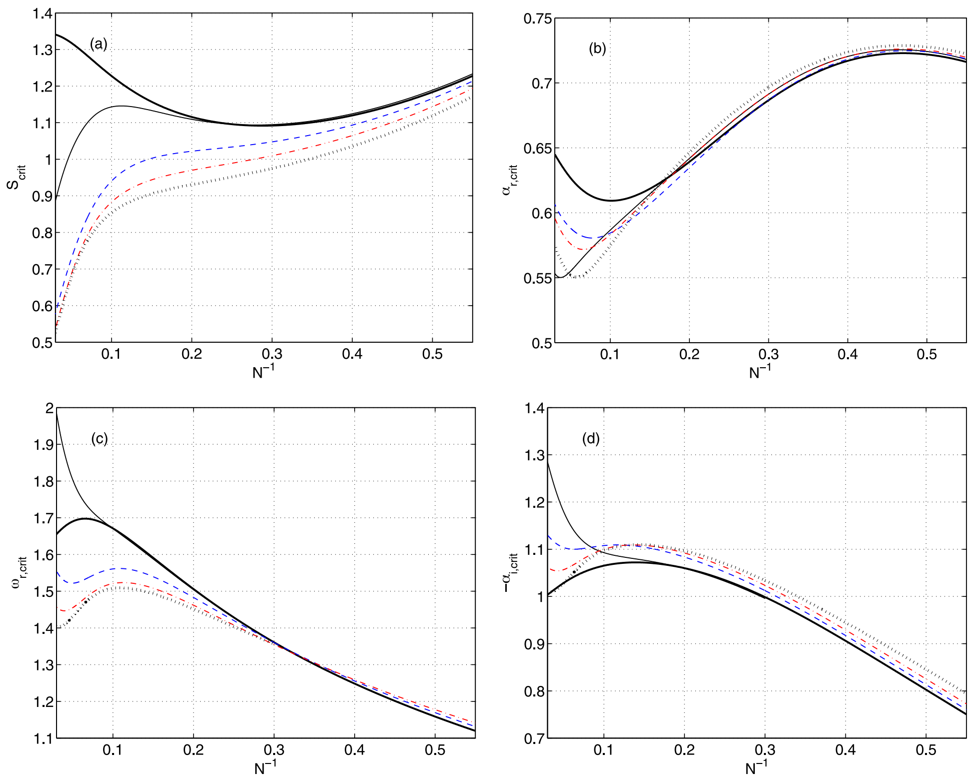

FIG. 6. Influence of *We* and N^{-1} on absolute instability, Re = 100; β = 0.7, L = 100, varicose, first jet-column mode; —— (thick), Newtonian; ——, *We* = 1; — —, *We* = 5; – · –, *We* = 10; · · ·, *We* = 20. (a) S_{crit}, (b) $\alpha_{r,crit}$, (c) $\omega_{r,crit}$, (d) $-\alpha_{i,crit}$.

example, in the current Re = 500 thin shear-layer jet, the shear-layer mode matches the behavior of the mixing layer; in the mixing layer, $\tilde{a}_{11}$ can be stabilizing as explained by Ray and Zaki.[7]

Reducing the Reynolds number from 500 to 100 substantially increases the destabilizing influence of viscoelasticity (compare Figures 3(a) and 6(a)). Generally, reducing the Reynolds number is expected to increase the influence of both the polymer and solvent contributions to the stress ($\frac{(1-\beta)}{Re}\tilde{a}_{ij}$ and $\frac{\beta}{Re}\frac{\partial \tilde{u}_i}{\partial x_j}$, respectively). Comparison of Figures 7(b) and 5(b) shows that, qualitatively, the influence of the polymer stress on the varicose jet-column mode is largely unchanged, but quantitatively, S_{crit} drops to much lower values. The reduction in Reynolds number does produce

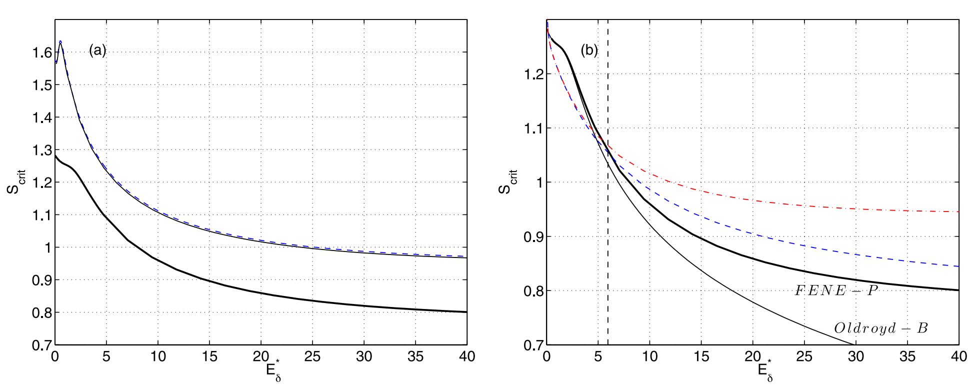

FIG. 7. Influence of elasticity on S_{crit}, Re = 100, β = 0.7, L = 100; N^{-1} = 0.07; (a) —— (thick), varicose jet-column mode; ——, tanh mixing layer; — —, varicose shear-layer mode; (b) varicose jet-column mode, ——, Oldroyd-B; —— (thick), FENE-P; — —, FENE-P with stress approximation; – · –, FENE-P with modified stress approximation; vertical dashed line, $\frac{We_\delta}{L}$ = 0.5.

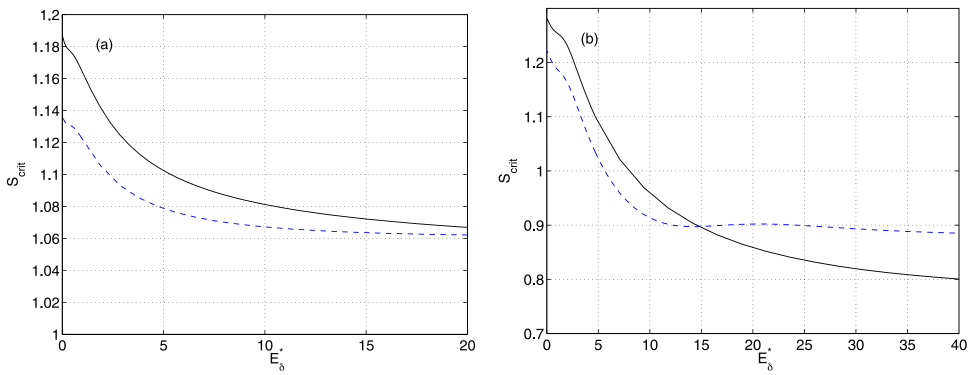

FIG. 8. Influence of solvent contribution to stress; $\beta = 0.7$, $L = 100$, $N^{-1} = 0.07$; ——, full solution; — —, reduced solvent contribution; (a) $Re = 500$, (b) $Re = 100$.

one notable qualitative change: the difference between the jet-column and shear-layer modes' S_{crit} curves is tangibly smaller at the lower Reynolds number (Figure 7(a)). The amplification of $\tilde{a}_{11}$ when $\frac{We_\delta}{L} \gtrsim 0.5$ strongly stabilizes the shear-layer mode when $Re = 500$ but becomes weakly destabilizing at $Re = 100$. Consequently, the shear-layer mode tracks the jet-column mode more closely at the lower Reynolds number.

We have assessed the importance of the solvent contribution to the stress by solving approximate equations with the stress modified to $\epsilon \frac{\beta}{Re} \frac{\partial \tilde{u}_i}{\partial x_j}$ with $\epsilon \leq 1$. Figure 8 shows results for S_{crit} with $\epsilon = 0.1$. Initially, when E^*_δ is small and non-Newtonian effects are insignificant, reducing ϵ also reduces S_{crit}, the viscous stress is stabilizing as expected. However, as elasticity increases, the influence of the viscous stress changes, and at sufficiently large values of the elasticity, the solvent contribution to the stress becomes destabilizing. The magnitude of this destabilizing effect is much larger at the lower Reynolds number. In contrast, the viscous stress is relatively insignificant for the shear-layer modes.

1. Influence of β, Re, and L

Up to this point, the viscosity ratio, β, and maximum extensibility, L, have been kept fixed while only two values of Re have been considered. We will now vary these parameters and assess how they affect the influence of elasticity on S_{crit} for the varicose jet-column mode with $N^{-1} = 0.07$. The influence of L is shown in Figure 9(a), and reducing the extensibility generally reduces the influence of viscoelasticity. When the shear rate is large, the base-state normal polymer stress scales as $\overline{A}_{11} \sim L^{4/3}$ while the $\tilde{a}_{11}$ amplification term scales as $\left(4\frac{\eta^2}{\mathcal{F}^2}\right)\overline{A}_{11} \sim L^{2/3}$. So, a reduction in L

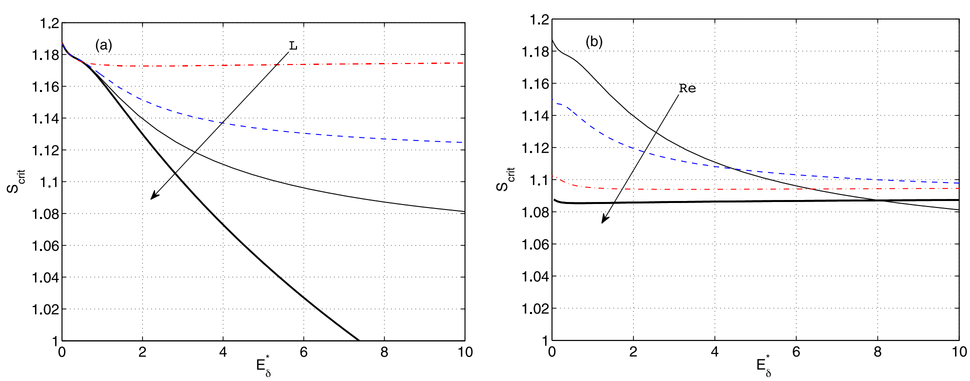

FIG. 9. S_{crit} for varicose jet-column mode, $\beta = 0.7$, $N^{-1} = 0.07$, (a) $Re = 500$; —— (thick), Oldroyd-B; ——, $L = 100$; — —, $L = 50$; – · –, $L = 10$; (b) $L = 100$; ——, $Re = 500$; — —, $Re = 1000$; – · –, $Re = 4000$; —— (thick), $Re = 10\,000$.

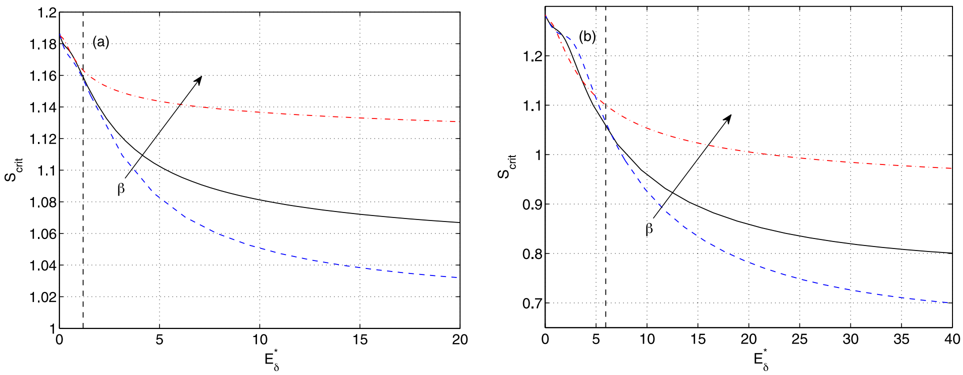

FIG. 10. Influence of β on varicose jet-column mode stability, $L = 100$, $N^{-1} = 0.07$; — —, $\beta = 0.5$; ——, $\beta = 0.7$; – · –, $\beta = 0.9$, (a) $Re = 500$, (b) $Re = 100$.

tends to reduce both the base-state and perturbation streamwise-normal polymer stresses. Additionally, reducing the extensibility reduces the extent of the Oldroyd-B region where viscoelasticity is destabilizing. For example, for the case shown in Figure 9(a), when $L = 10$ and $\frac{We_\delta}{L} \le 0.5$, the elasticity falls in the range, $E^*_\delta \le 0.12$, and is too small for the stability results to be significantly affected.

Increasing the Reynolds number (Figure 9(b)) moves the stability results toward those for an inviscid jet. Absolute instability is largely independent of elasticity when $Re \gtrsim 4000$. A similar trend is seen when the viscosity ratio is increased (Figure 10). In this case, as β is increased towards one, the stability results move towards those for a Newtonian jet. The influence of β is most clearly seen in the finite shear rate region, $\frac{We}{L} \gtrsim 0.5$. In the Oldroyd-B region, most of the influence of viscoelasticity is captured by the elasticity, E^*_δ (which follows from Eq. (7)).

B. Thick shear layer results and comparisons to Rallison and Hinch

RH[6] analyzed the temporal stability of Oldroyd-B jets with parabolic velocity profiles, and we now consider how their study relates to the results presented here. We must first connect the parabolic profile,

$$\overline{U}_1 = \begin{cases} 2(1 - \frac{x_2^2}{2}) & x_2 < \sqrt{2} \\ 0 & x_2 > \sqrt{2} \end{cases}, \tag{8}$$

to the profiles used here (Eq. (4)). The momentum thickness of the parabolic profile is $\delta^p = 2\sqrt{2}/15 \approx 0.189$; a profile given by Eq. (4) matches this thickness when $N^{-1} = 0.555$, and a comparison of these profiles is shown in Figure 11(a). Following RH, we now consider solutions to the elastic Rayleigh equation introduced in Ref. 5,

$$\frac{d}{dx_2}\left\{\left[\tilde{U}^2 - 2E^*\left(\frac{d\overline{U}_1}{dx_2}\right)^2\right]\frac{d\Phi}{dx_2}\right\} - \alpha^2\left[\tilde{U}^2 - 2E^*\left(\frac{d\overline{U}_1}{dx_2}\right)^2\right]\Phi = 0. \tag{9}$$

The elastic Rayleigh equation can be obtained from approximate momentum equations (7) presented earlier by neglecting the solvent contribution to the stress (i.e., the right-hand side) and taking the limit, $L \to \infty$. Figure 11(b) shows temporal stability results for this equation using both the smooth ($N^{-1} = 0.555$, $S = 1$) and parabolic velocity profiles. The smooth-profile results reproduce the most important qualitative trends discussed by RH: (1) The sinuous mode is more-unstable in the inviscid limit ($E^* \to 0$) but is completely stabilized by elasticity; (2) The growth rate of the varicose mode is reduced by elasticity but the mode is not fully stabilized, and it thus becomes the most dangerous mode as E^* increases. The smooth and parabolic profiles do differ for the varicose mode at small elasticities. There, the parabolic-profile results are influenced by the interaction between

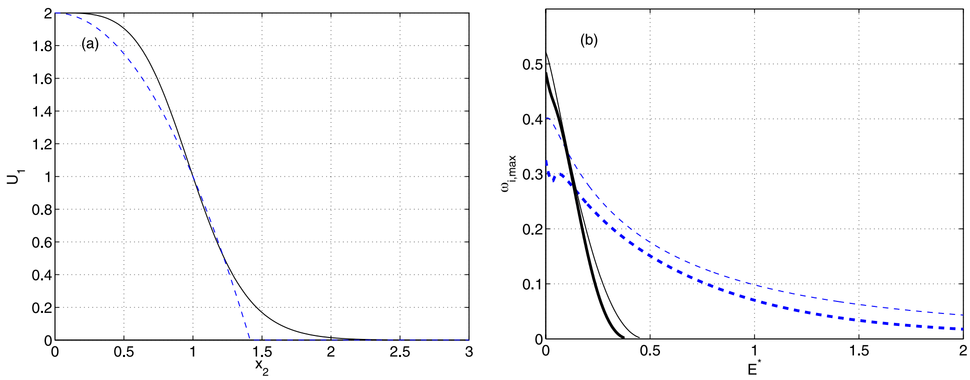

FIG. 11. (a) "Thick" base-flow velocity profiles; ——, $N^{-1} = 0.555$; — —, parabolic profile; (b) temporal stability results: maximum temporal growth rate for elastic Rayleigh equation with parabolic (thick) and smooth (thin) velocity profiles; ——, sinuous; — —, varicose.

two waves as discussed in detail by RH. The "kink" seen for the varicose mode small-E^* result in Figure 11(b) is due to this interaction; smooth profiles where the base-state normal stress varies continuously do not seem to produce this behavior,[29] and in the following we will only consider the "thick" smooth profile with $N^{-1} = 0.555$ and $S = 1$.

For spatially developing flows, temporal stability results indicate whether the flow is unstable, and spatiotemporal results are needed to determine the type of instability.[9] For the sinuous mode with the smooth base-flow profile, when $E^* < 0.5$, $S_{crit} > 1$, and the flow is convectively unstable. Then, spatial analysis (where ω is real and α is complex) is appropriate, and the resulting maximum spatial growth rate, $-\alpha_{i,max}$, is shown in Figure 12(a). The spatial and temporal stability results for the sinuous mode are very similar, but the varicose mode exhibits more complicated behavior. Figure 12(b) shows the temporal growth rate of the varicose saddle-point mode. There is a small region of (weak) absolute instability when $\omega_i > 0$. Consequently, in Figure 12(a), spatial stability results for α_i are shown for $E^* < 0.187$ and $E^* > 0.336$ while absolute instability results are shown for $0.187 < E^* < 0.336$. There are a few important differences from the temporal results: the varicose mode has become the most-dangerous mode over the entire range of elasticities, there is now a small region of absolute instability, and there is a "plateau" at small E^* where the varicose-mode growth rate varies little. Beyond the region of absolute instability, $E^* > 0.336$, temporal and spatial results for the varicose mode are similar, and elasticity is stabilizing as explained by RH. For smaller elasticities, $E^* < 0.187$, the spatial, temporal, and saddle-point varicose modes all respond differently to elasticity. Similar behavior was seen for the Oldroyd-B mixing layer. When E^* is

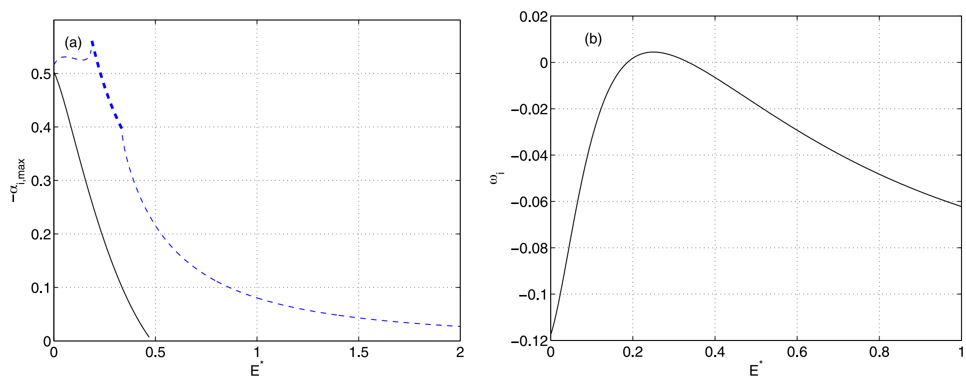

FIG. 12. Spatial and spatiotemporal instability results for elastic Rayleigh equation; (a) spatial results: maximum spatial growth rate; ——, sinuous; — —, varicose; — — (thick) varicose, absolute instability; (b) temporal growth rate of varicose absolute instability.

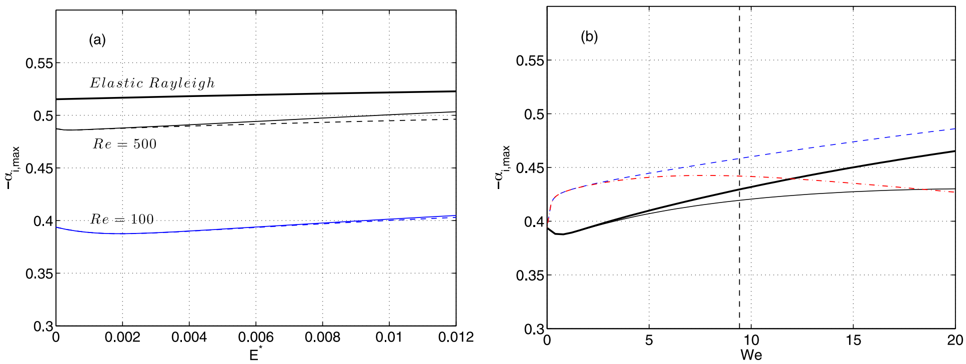

FIG. 13. Spatial stability results: maximum spatial growth rate for varicose modes, (a) —— (thick), elastic Rayleigh; ——, FENE-P; — —, Oldroyd-B; (b) $Re = 100$; ——, Oldroyd-B; —— (thick), FENE-P; — —, FENE-P with stress approximation; – · –, FENE-P with modified stress approximation; vertical dashed line, $\frac{We_\delta}{L} = 0.5$.

large, the elasticity behaves like a stabilizing surface tension,[5] and temporal and spatiotemporal analyses both show a reduction in growth rate. However, at smaller elasticities when inertial and viscoelastic effects are the same order-of-magnitude, spatiotemporal results indicate that polymers can exhibit a destabilizing influence while temporal analysis always predicts stabilization.[7]

At first glance, these results seem to be very different to those shown for thick shear layers in Figures 3 and 6. All of the FENE-P results shown earlier were for Weissenberg numbers in the range, $We < 20$. For $Re = 500$ and $\beta = 0.7$, this corresponds to $E^* < 0.012$, and elastic-Rayleigh, Oldroyd-B, and FENE-P results all show little sensitivity to elasticity in this range (Figure 13(a)). At $Re = 100$, FENE-P spatial-stability results do show a modest destabilization at high Weissenberg numbers (Figure 13(b)) which is similar to the spatiotemporal results for S_{crit} in Figure 6(a). Interestingly, these FENE-P results are more sensitive to elasticity than the Oldroyd-B results. This difference can be understood by repeating the analysis used for the thin shear layer case. The influence of the perturbation normal stress is isolated by comparing full and simplified solutions to approximate equations (7). In Figure 13(b), we see that removing the amplification of $\tilde{a}_{11}$ shifts the FENE-P solution towards the Newtonian result. Earlier, we had seen that at finite shear rates, the difference between the FENE-P and Oldroyd-B results is dictated by the balance between the reduction in the base-state normal stress and the amplification of $\tilde{a}_{11}$. Here, we see that the destabilizing influence of the perturbation stress is sufficiently strong to "push" the FENE-P growth rate above the Oldroyd-B result despite the (relative) reduction in the base-state stress.

In summary, our thick-profile results tend to show different behaviors from that observed in RH due to (1) the use of a smooth base flow profile, (2) the use of spatiotemporal analysis, (3) the inclusion of finite-extensibility effects via the FENE-P model, and (4) our focus on a relatively moderate range of elasticities. Additionally, the consideration of a range of shear-layer thicknesses indicates that viscoelastic effects are substantially stronger when the initial jet shear-layers are thin.

IV. CONCLUDING REMARKS

The influence of viscoelasticity on the onset of local absolute instability in planar FENE-P jets has been investigated. The first varicose jet-column mode was found to control the onset of absolute instability, and we focused on jet profiles with thin shear layers where viscoelasticity was found to have a destabilizing influence. The nature of this influence depends on both the elasticity and the shear rate. As in the mixing layer, the parameter space can be divided into Oldroyd-B and finite shear-rate regions. In the Oldroyd-B region, when the elasticity (based on the momentum thickness) is $O(1)$ and the shear rate is small, viscoelasticity produces a destabilizing influence on both the shear-layer and jet-column modes. When the shear rate is $O(1)$ or larger, the behavior of the jet-column and shear-layer modes differs. Both the polymer and solvent contributions to the stress are then destabilizing for the varicose jet-column mode. The combined influence of these destabilizing effects leads to a single-stream jet becoming absolutely unstable when the jet shear layer is sufficiently thin and elasticity is sufficiently large.

Reducing the Reynolds number from 500 to 100 enhances the destabilizing influence of viscoelasticity on the varicose jet-column mode. The qualitative trends observed at $Re = 500$ remain in place, and this enhancement is driven by the increase in the relative importance of the (destabilizing) polymer and solvent stresses when the Reynolds number is reduced. Additionally, our calculations show that at $Re = 100$, single-stream jets become absolutely unstable over a sizable portion of the parameter space. This should be contrasted with the results of Rees and Juniper[12] which show that reducing Re results in the suppression of absolute instability in confined Newtonian jets and wakes. However, due to the locally parallel base flow assumption in our analysis, complementary global stability calculations[23,24] (which account for shear-layer spreading) are needed to fully assess the influence of viscoelasticity at lower Reynolds numbers.

Studies of viscoelastic free shear layers have typically been motivated by drag-reduction in turbulent pipe and channel flows[30] and have largely sought a damping or stabilizing influence from polymer additives (e.g., Hoyt[31]). Initial temporal stability studies[5,6] indicated that viscoelasticity was usually stabilizing; however, spatiotemporal stability calculations show greater complexity.[7] In this study, our results indicate that viscoelasticity does not stabilize absolute instability in planar jets. Rather, in certain regions of the parameter space (small N^{-1}, moderate Re and β), absolute instability is substantially enhanced which suggests that a different perspective may be desirable in this regime (e.g., a shift in focus from transition delay to instability enhancement and mixing). Convective instabilities may also produce unexpected behavior and require further study. This work provides a necessary foundation for future spatial stability studies by establishing when viscoelastic planar jets are convectively or absolutely unstable.

An important unanswered question is whether the trends predicted here are observed in experiments or direct simulations. Experimental studies of viscoelastic jets have generally focused on high-Reynolds number turbulent flows of dilute polymer solutions (e.g., Refs. 30 and 32), while our results indicate that the most interesting effects will be found at "transitional" Reynolds numbers ($Re \lesssim 500$) with semi-dilute solutions. We are also not aware of any direct simulations of unsteady viscoelastic jets. The flow-visualization study of Fruman *et al.*[33] did find the appearance of instability in round polymeric jets (expelled into water) when $Re \gtrsim 50$; however, it is not possible to discern if these instabilities are "absolute." In general, the presence of a sufficiently large region of absolute instability should lead to the development of large-amplitude synchronized oscillations. Linear stability results for S_{crit} and ω_r (such as those presented in Figure 6) provide estimates for the onset and frequency of these oscillations,[34] and these estimates should both guide and be compared to future experimental and numerical studies of polymeric jets.

APPENDIX: FURTHER DETAILS ON FORMULATION

The full governing equations are

$$\mathbf{A}\tilde{f} = \mathbf{B}\frac{d\tilde{f}}{dx_2}, \tag{A1}$$

with

$$\mathbf{A} = \begin{bmatrix} 0 & 1 & 0 & 0 \\ \Gamma Re - \mathcal{R}_3(1-\beta) + \alpha^2\beta & -(1-\beta)\mathcal{R}_2 & Re\dfrac{dU_1}{dx_2} - (1-\beta)\mathcal{R}_4 & i\alpha Re \\ -i\alpha & 0 & 0 & 0 \\ (1-\beta)\mathcal{S}_3 & (1-\beta)\mathcal{S}_2 - i\alpha\beta & -\Gamma Re - \alpha^2\beta + (1-\beta)\mathcal{S}_4 & 0 \end{bmatrix},$$

$$\mathbf{B} = \begin{bmatrix} 1 & 0 & 0 & 0 \\ 0 & (1-\beta)\mathcal{R}_1 + \beta & 0 & 0 \\ 0 & 0 & 1 & 0 \\ 0 & -(1-\beta)\mathcal{S}_1 & 0 & Re \end{bmatrix}, \ \Gamma \equiv i(\alpha\overline{U}_1 - \omega).$$

The components of $\mathcal{R}_m$ and $\mathcal{S}_m$ are used to relate the polymer stress perturbations to $\tilde{f}$,

$$i\alpha\tilde{a}_{11} + \frac{d\tilde{a}_{12}}{dx_2} = \mathcal{R}_1\frac{d^2\tilde{u}_1}{dx_2^2} + \mathcal{R}_2\frac{d\tilde{u}_1}{dx_2} + \mathcal{R}_3\tilde{u}_1 + \mathcal{R}_4\tilde{u}_2, \tag{A2a}$$

$$i\alpha\tilde{a}_{12} + \frac{d\tilde{a}_{22}}{dx_2} = \mathcal{S}_1\frac{d^2\tilde{u}_1}{dx_2^2} + \mathcal{S}_2\frac{d\tilde{u}_1}{dx_2} + \mathcal{S}_3\tilde{u}_1 + \mathcal{S}_4\tilde{u}_2. \tag{A2b}$$

Expressions for $\mathcal{R}_m$ and $\mathcal{S}_m$ are obtained from the linearized FENE-P equations. The perturbation conformation tensor components, $\tilde{c}_m = [\tilde{c}_{11}\ \tilde{c}_{12}\ \tilde{c}_{22}\ \tilde{c}_{33}]^T$, are related to the velocity, $\tilde{g}_m = \left[\frac{d\tilde{u}_1}{dx_2}\ \tilde{u}_1\ \tilde{u}_2\right]^T$, by

$$F_{mn}\tilde{c}_n = We\, G_{mn}\tilde{g}_n, \tag{A3}$$

$$F_{mn} = \begin{bmatrix} We\,\Gamma + H_0(1+\overline{H}_{11}) & -2\tau & H_0\overline{H}_{11} & \overline{H}_{11} \\ H_0\overline{H}_{12} & We\,\Gamma + H_0 & -\tau + H_0\overline{H}_{12} & \overline{H}_{12} \\ H_0\overline{H}_{22} & 0 & We\,\Gamma + H_0(1+\overline{H}_{22}) & \overline{H}_{22} \\ H_0\overline{H}_{33} & 0 & H_0\overline{H}_{33} & We\,\Gamma + H_0(1+\overline{H}_{33}) \end{bmatrix},$$

$$G_{mn} = \begin{bmatrix} 2\overline{C}_{12} & 2i\alpha\overline{C}_{11} & -\dfrac{d\overline{C}_{11}}{dx_2} \\ \overline{C}_{22} & 0 & -\dfrac{d\overline{C}_{12}}{dx_2} + i\alpha\overline{C}_{11} \\ 0 & -2i\alpha\overline{C}_{22} & 2i\alpha\overline{C}_{12} - \dfrac{d\overline{C}_{22}}{dx_2} \\ 0 & 0 & -\dfrac{d\overline{C}_{33}}{dx_2} \end{bmatrix},$$

where $\tau = We\frac{d\overline{U}_1}{dx_2}$, $H_0 = \frac{L^2-3}{L^2-\overline{C}_{kk}}$, and $\overline{H}_{ij} = \frac{\overline{C}_{ij}}{L^2-\overline{C}_{kk}}$. We invert F_{mn} to get $\tilde{c}_m = D_{mn}\tilde{g}_n$, $D_{mn} = We(F_{mp})^{-1}G_{pn}$. We then have, $\frac{d\tilde{c}_m}{dx_2} = \frac{dD_{mn}}{dx_2}\tilde{g}_n + D_{mn}\frac{d\tilde{g}_n}{dx_2}$. The perturbation stress, $\tilde{a}_m = [\tilde{a}_{11}\ \tilde{a}_{12}\ \tilde{a}_{22}]^T$ is related to $\tilde{c}_n$ by

$$\tilde{a}_m = \frac{H_0}{We}E_{mn}\tilde{c}_n, \tag{A4}$$

$$E_{mn} = \begin{bmatrix} 1+\overline{H}_{11} & 0 & \overline{H}_{11} & \overline{H}_{11} \\ \overline{H}_{12} & 1 & \overline{H}_{12} & \overline{H}_{12} \\ \overline{H}_{22} & 0 & 1+\overline{H}_{22} & \overline{H}_{22} \end{bmatrix},$$

so $\tilde{a}_m = M_{mp}\tilde{g}_p$, $M_{mp} = \frac{H_0}{We}E_{mn}D_{np}$, and the desired expressions for $\mathcal{R}_m$ and $\mathcal{S}_m$ are given by

$$\mathcal{R}_m = \begin{bmatrix} M_{21} \\ i\alpha M_{11} + N_{21} + M_{22} \\ i\alpha(M_{12} - M_{23}) + N_{22} \\ i\alpha M_{13} + N_{23} \end{bmatrix}, \mathcal{S}_m = \begin{bmatrix} M_{31} \\ i\alpha M_{21} + N_{31} + M_{32} \\ i\alpha(M_{22} - M_{33}) + N_{32} \\ i\alpha M_{23} + N_{33} \end{bmatrix}, N_{mn} = \frac{dM_{mn}}{dx_2}. \tag{A5}$$

[1] O. Cadot and S. Kumar, "Experimental characterization of viscoelastic effects on two- and three-dimensional shear instabilities," J. Fluid Mech. **416**, 151–172 (2000).
[2] M. Sahin and R. G. Owens, "On the effects of viscoelasticity on two-dimensional vortex dynamics in the cylinder wake," J. Non-Newtonian Fluid Mech. **123**, 121–139 (2004).
[3] D. Richter, E. S. G. Shaqfeh, and G. Iaccarino, "Floquet stability analysis of viscoelastic flow over a cylinder," J. Non-Newtonian Fluid Mech. **166**, 554–565 (2011).
[4] C. J. Pipe and P. A. Monkewitz, "Vortex shedding in flows of dilute polymer solutions," J. Non-Newtonian Fluid Mech. **139**, 54–67 (2006).
[5] J. Azaiez and G. M. Homsy, "Linear stability of free shear flow of viscoelastic liquids," J. Fluid Mech. **268**, 37–69 (1994).
[6] J. M. Rallison and E. J. Hinch, "Instability of a high-speed submerged elastic jet," J. Fluid Mech. **288**, 311–324 (1995).
[7] P. K. Ray and T. A. Zaki, "Absolute instability in viscoelastic mixing layers," Phys. Fluids **26**, 014103 (2014).

[8] S. Jendoubi and P. J. Strykowski, "Absolute and convective instability of axisymmetric jets with external flow," Phys. Fluids **6**, 3000 (1994).
[9] P. Huerre and P. A. Monkewitz, "Local and global instabilities in spatially developing flows," Annu. Rev. Fluid Mech. **22**, 473–537 (1990).
[10] M.-H. Yu and P. A. Monkewitz, "The effect of nonuniform density on the absolute instability of two-dimensional inertial jets and wakes," Phys. Fluids A **2**, 1175 (1990).
[11] M.-H. Yu and P. A. Monkewitz, "Oscillations in the near field of a heated two-dimensional jet," J. Fluid Mech. **255**, 323–347 (1993).
[12] S. J. Rees and M. P. Juniper, "The effect of confinement on the stability of viscous planar jets and wakes," J. Fluid Mech. **656**, 309–336 (2010).
[13] C. M. White and M. G. Mungal, "Mechanics and prediction of turbulent drag reduction with polymer additives," Ann. Rev. Fluid Mech. **40**, 235–256 (2008).
[14] S. Jin and L. R. Collins, "Dynamics of dissolved polymer chains in isotropic turbulence," New J. Phys. **9**, 360 (2007).
[15] R. B. Bird, P. J. Dotson, and N. L. Johnson, "Polymer solution rheology based on a finitely extensible bead-spring chain model," J. Non-Newtonian Fluid Mech. **7**, 213–235 (1980).
[16] Q. Zhou and R. Akhavan, "A comparison of FENE and FENE-P dumbbell and chain models in turbulent flow," J. Non-Newtonian Fluid Mech. **109**, 115–155 (2003).
[17] R. B. Bird, C. F. Curtiss, R. C. Armstrong, and O. Hassager, *Dynamics of Polymeric Fluids* (Wiley, New York, 1987).
[18] P. Meliga, D. Sipp, and J.-M. Chomaz, "Absolute instability in axisymmetric wakes: Compressible and density variation effects," J. Fluid Mech. **600**, 373–401 (2008).
[19] P. A. Monkewitz, "A note on vortex shedding from axisymmetric bluff bodies," J. Fluid Mech. **192**, 561–575 (1988).
[20] R. Sureshkumar, A. N. Beris, and R. A. Handler, "Direct numerical simulation of the turbulent channel flow of a polymer solution," Phys. Fluids **9**, 743–755 (1997).
[21] A. Michalke, "Survey of jet instability theory," Prog. Aerosp. Sci. **21**, 159–199 (1984).
[22] P. A. Monkewitz, "The absolute and convective nature of instability in two-dimensional wakes at low Reynolds numbers," Phys. Fluids **31**, 999–1006 (1988).
[23] M. P. Juniper, O. Tammisola, and F. Lundell, "The local and global stability of confined planar wakes at intermediate Reynolds number," J. Fluid Mech. **686**, 218–238 (2011).
[24] J.-M. Chomaz, "Global instabilities in spatially developing flows: Non-normality and nonlinearity," Annu. Rev. Fluid Mech. **37**, 357–392 (2005).
[25] S. D. Conte, "The numerical solution of linear boundary value problems," SIAM Rev. **8**, 309–321 (1966).
[26] P. Huerre and P. A. Monkewitz, "Absolute and convective instabilities in free shear layers," J. Fluid Mech. **159**, 151–168 (1985).
[27] L. Xi and M. D. Graham, "Turbulent drag reduction and multistage transitions in viscoelastic minimal flow units," J. Fluid Mech. **647**, 421–452 (2010).
[28] Y. Dubief, C. M. White, V. E. Terrapon, E. S. G. Shaqfeh, P. Moin, and S. K. Lele, "On the coherent drag-reducing and turbulence-enhancing behaviour of polymers in wall flows," J. Fluid Mech. **514**, 271–280 (2004).
[29] J. C. Miller, "Shear flow instabilities in viscoelastic fluids," Ph.D. dissertation (University of Cambridge, 2005).
[30] S. J. Barker, "Laser-doppler measurements on a round turbulent jet in dilute polymer solutions," J. Fluid Mech. **60**, 721–731 (1973).
[31] J. W. Hoyt, "Effect of polymer additives on jet cavitation," J. Fluids Eng. **98**, 106–111 (1976).
[32] N. S. Berman and H. Tan, "Two-component laser doppler velocimeter studies of submerged jets of dilute polymer solutions," AIChE J. **31**, 208–215 (1985).
[33] D. H. Fruman, P. Perrot, and J. Bouguechal, "On the swelling of submerged jets of dilute and semi-dilute polymer solutions," Chem. Eng. Commun. **27**, 101–118 (1984).
[34] P. A. Monkewitz, P. Huerre, and J.-M. Chomaz, "Global linear stability analysis of weakly non-parallel shear flows," J. Fluid Mech. **251**, 1–20 (1993).